Spectral characteristics of ionospheric disturbances over the Southwestern Pacific from the January 15, 2022 Tonga eruption and tsunami

Jessica N. Ghent* and Brendan W. Crowell

Department of Earth and Space Sciences
University of Washington
Johnson Hall Rm-070, Box 351310
4000 15th Ave NE
Seattle, WA 98195-1310

*Corresponding author, jghent@uw.edu

Key Points

- **The eruption and tsunami from Hunga caused acoustic gravity waves in the ionosphere**
- **Distinct phase arrivals for the supersonic wave, Lamb wave, and tsunami are visible**
- **After the Lamb wave, the frequency of the tsunami wave is higher and propagates at a faster speed**

Abstract

On January 15, 2022, Tonga's Hunga volcano violently erupted, generating a tsunami that killed at least three people. Acoustic-gravity waves propagated by both the eruption and tsunami caused global complex ionospheric disturbances. In this paper, we study the nature of these disturbances from Global Navigation Satellite System observables over the southwestern Pacific. After processing data from 818 ground stations, we find that supersonic acoustic waves, Lamb waves, and tsunamis are all detected, with filtered magnitudes between 1 and 7 Total Electron Content units. Disturbances appear superpositioned up to ~1000 km from Hunga and are distinct beyond this distance. Within ~2000 km, signals have an initial low-frequency pulse that transition to higher frequencies. The arrival of tsunami-generated ionospheric disturbances coincides with deep-ocean observations. Lastly, we find that the Lamb wave and initial tsunami propagated minutes apart at the same velocity, leading to earlier land arrivals than predicted.

Plain Language Summary

The January 15, 2022 eruption of Hunga volcano and subsequent tsunamis sent powerful atmospheric waves into the ionosphere (a layer of Earth's atmosphere that extends from ~70 km above Earth out to space and is deformed by energy emitted from events like volcanic eruptions, tsunamis, earthquakes, tornadoes, hurricanes, and large man-made explosions). Using Global Positioning System satellite data, we measure these deformations in the ionosphere over the southwestern Pacific region to infer which phase of the eruption and tsunami contributed to each ionospheric disturbance. We quantify the speeds at which these disturbances travel and validate inferred tsunami velocities against ocean pressure sensors. Our analysis supports the early tsunami arrivals reported in many locations and suggests that strong pressure waves from the eruption enhanced tsunami speeds and wave heights.

Keywords

- Ionosphere
- Volcanic eruption
- Tsunami
- GNSS

1. Introduction

On January 15, 2022, a violent eruption occurred at Hunga, a small marine volcano in the Tonga archipelago approximately 65 km north of the main island of Tongatapu. Previously existing as two distinct landmasses, the islands Hunga Tonga and Hunga Ha'apai merged in a 2014-2015 eruption sequence that connected both sides of Hunga subaerially. Volcanic activity renewed in December 2021 and escalated on January 14, 2022 with an eruption that once again separated the two islands and brought the crater below the ocean's surface. The following morning, the climactic eruption occurred at 04:14 UTC and continued in a complex sequence of at least five explosions for the next 20 minutes, concluding with a final large explosion at ~08:31 UTC (Astafyeva et al., 2022; Matoza et al., 2022). This event generated incredibly powerful acoustic-gravity (AG) waves, the largest of which - the Lamb wave, an AG wave traveling in the direction of wave propagation along Earth's surface and in the normal plane near the speed of sound in the lower atmosphere (Lamb, 1911) - crossed the globe numerous times over the next three days, something which has not been observed since the 1883 eruption of Krakatoa (Matoza et al., 2022; Zhang et al., 2022). Furthermore, the Hunga eruption generated a tsunami that reached coastlines around the Pacific basin; elevated sea levels were also observed in the Mediterranean and Caribbean seas as well as in the Indian and Atlantic oceans (Carvajal et al., 2022). Both the eruption and tsunami produced AG waves that propagated into the ionosphere, resulting in traveling ionospheric disturbances (TIDs) that were also witnessed across the globe.

The ionosphere, a mid- to upper-atmospheric layer containing ions and free electrons, is disturbed by natural events such as volcanic eruptions and tsunamis that propel AG waves along and upward from Earth's surface (Hines, 1972). These perturbations can be tracked in the ionosphere to detect remote events, determine the magnitude of events, and quantify metrics such as propagation velocities and arrival times (Astafyeva, 2019; Huang et al., 2019, and references therein; Manta et al., 2021). In the past two decades, many advancements have been made in ionospheric analysis. The development of the Variometric Approach for Real-Time Ionosphere Observation (VARION) algorithm by Savastano et al. (2017) demonstrated the potential for real-time ionospheric tracking of natural hazards like tsunamis. Further studies have shown that ionospheric signals can be separated into frequency peaks that are attributed to distinct phases of an eruption (Dautermann et al., 2009).

In this manuscript, we analyze ionospheric disturbances from the Hunga eruption and ensuing tsunamis recorded by Global Navigation Satellite System (GNSS) observations of total electron content (TEC) throughout the southwestern Pacific basin. The dispersive nature of the ionosphere to radio frequency signals allows for the extraction of this signal with dual-frequency GNSS observations. We look at the moveout of disturbances to isolate key phases in the eruption and tsunamis. We investigate the spectral characteristics of the signal to validate the timing and occurrence of separation between the Lamb wave and initial tsunami arrivals. Finally, we look at arrival times of the first peak at DART (Deep-ocean Assessment and Reporting of Tsunamis) buoys around New Zealand to show the correspondence between the tsunami arrival and the high-frequency phase arrival in the ionosphere.

2. Data and Methods

We focus our analysis on stations in the southwestern Pacific Ocean within 5000 km from the volcano. Within this region, there are three ultra-dense GNSS networks: Australia, New Zealand, and Hawaii. Though the region within ~2000 km is not densely instrumented due to minimal available land, observations in Samoa, Tonga, and other outlying islands provide excellent observations on many satellites. We obtained raw GNSS data in RINEX2 format from UNAVCO, the International GNSS Service (IGS), GNS New Zealand, and Geoscience Australia at either 15- or 30-second sample rates. The orientation of the New Zealand network is particularly advantageous since stations are oriented roughly along the back-azimuth to Tonga, which allows for better tracking of the moveout from the volcano; the networks in Australia and Hawaii are oriented orthogonal to this and have phase arrivals at similar times. In total, we processed data from 818 stations, with most either in Australia (563) or New Zealand (195).

GNSS data was processed using SNIVEL_ION, a revised version of Satellite Navigation-derived Instantaneous VELocities, or SNIVEL (Crowell, 2021). SNIVEL_ION utilizes the time-differenced geometry-free combination of L1 and L2 phase observables on the GPS constellation. The raw output from SNIVEL_ION is in variometric (i.e., differential) TEC units (vTEC; TEC/unit time) along the slant from satellite to receiver. We processed each station from 03:00 UTC to the end of the day, however, most of our analysis is within 12 hours of the eruption at 04:14 UTC. After we obtained our vTEC observations for each station-satellite pair, we first removed an 8th degree polynomial fit to get rid of large-scale drifts in the time series before numerically integrating to absolute TEC (aTEC) values. We then applied a bandpass, 4-pole, zero-phase, Butterworth filter between 0.5 and 10 mHz, which corresponds to periods between 100 and 2000 s. We required a minimum of 240 continuous data points for each station-satellite pair to include it in our dataset. This value was arbitrarily chosen and represents two continuous hours of data for 30-second sample rate data. We also excluded observations below an elevation mask of 18 degrees. Since SNIVEL_ION does not include an outlier filter, we manually inspected all of the waveforms with a filtered aTEC value greater than 5 to remove gross outliers from our analysis; note that many non-outlier observations with aTEC values greater than 5 were present. After removing outlier satellite-receiver pairs, we were left with 9.7 million time series points. Of the total satellite-receiver time series points, 5.6% are within 2000 km of the volcano, 21.2% between 2000-3000 km, 31.9% between 3000-4000 km, and 41.7% greater than 4000 km. To investigate the frequency dependence of the aTEC perturbations for key station-satellite pairs, we performed a wavelet transform using a Morlet wavelet. We only looked at the wavelet transform in the period range between 100 and 2000 s to correspond with the bandpass filter we applied to the aTEC time series. In processing this TEC data, we determined the ionospheric piercing point (IPP) using the Klobuchar model and an assumed thin layer height of 350 km (Klobuchar, 1987). The sub-ionospheric distance used throughout is the distance from the volcano to the surface projection of the IPP. The standard error assumption for variometric TEC is less than 0.03 TECu (Coster et al., 2012; Zhang et al., 2022); however, as the errors are complex and frequency-dependent, we use this value as an approximate uncertainty. Further analysis is required to establish more precise uncertainty estimates of the colored noise structure. All TEC files created in this study are available from Ghent & Crowell (2022).

In addition to the TEC data, we also used data from several DART buoys owned and operated by GNS New Zealand to compare tsunami arrival times with phase arrivals in the ionosphere. For this analysis, we downloaded 15-second sample rate data and bandpassed the data similarly to the TEC data to primarily remove long-period tidal signals.

3. Results and Discussion

Figure 1 shows dense TID arrivals over New Zealand and Australia, while also highlighting the sparsity of data over most of the southwestern Pacific.

Close to the source, TIDs arrive in the ionosphere within minutes of the eruption. Filtered disturbances appear to be superpositioned up to a distance of ~1000 km from the volcano (Figure 2). The SAMO station on Samoa (837 km northeast of Hunga; the IPP for satellite G23 is 300 km away at the time of the eruption) recorded a disturbance that peaks at 04:38 UTC at an amplitude of 6.3 TECu (Figure 2a). Wavelet analysis shows one dominant signal over a broad range of periods that is heavily concentrated in the lower end of the range, with a peak concentration in period at 923 s (Figure 2d) and a mean power peak at 69 (Figure 2g). Note that the mean power absolute units (Figure 2g-i) are dependent on the particular design of the wavelet transform, but all wavelets in Figure 2 have the same design and are in the same units. Both the period and mean power peaks occur at the same time as the maximum TECu. Our peak TECu is slightly larger than others recently published (Matoza et al., 2022; Themens et al., 2022; Zhang et al., 2022), but all are the same order of magnitude; differences in TEC values are due to individual filtering/processing methods. Regardless, this amplitude of ionospheric perturbation is significantly larger than has ever been observed, demonstrating the immense power of the Hunga eruption.

Lamb- and tsunami-induced TIDs become distinct on Raoul Island (~1000 km southwest of Hunga), although there appears to be some overlap remaining. Separation of the TIDs is inferred by the arrival of the Lamb wave, which peaks at 05:17 UTC at an amplitude of 3.5 TECu, followed closely by the initial tsunami which peaks at 05:41 UTC at an amplitude of 5.0 TECu (Figure 2b). Looking at the wavelet analysis for RAUL, the peak period is 1423 s at 05:30, which drops to 1073 s at 05:42 (Figure 2e); this supports the interpretation that we are witnessing separation of the Lamb and tsunami TIDs at this distance. The mean power for each TID peaks at 24 and 36 (Figure 2h). TID separation is even clearer over New Zealand at station 2406 (2175 km southwest of Hunga), with the arrival time of the actual tsunami dividing each disturbance (Figure 2c). The Lamb wave's TID peaks at 06:02 UTC at an amplitude of 0.70 TECu, while the tsunami's TID peaks at 06:43 UTC at a maximum amplitude of 1.1 TECu. In the wavelet analysis for 2406, the two disturbances show peak concentrations in period around ~1800 s and ~800 s that are clearly separated by the actual tsunami's arrival time (Figure 2f). The mean power for each TID peaks at 1.6 and 2, with a local minimum at the time of the tsunami's arrival (Figure 2i). Much of the loss of power can be explained through geometrical spreading, but some may be due to the spreading out of the Lamb and tsunami disturbances that were previously superimposed at shorter distances.

Moveout of the TIDs is visualized in a distance-time plot of TEC time series across New Zealand (Figure 3a). Here we see TEC time series gathered by individual receivers and projected radially down from IPPs along the ground path of satellite G10. Again, the first disturbance is interpreted to be from the Lamb wave, while the second is inferred to be from the initial tsunami wave. First peak DART arrivals from Gusman & Roger (2022) placed atop TID moveouts show that the actual tsunami and tsunami-generated TIDs have nearly identical propagation velocities. An abrupt change in wavelength and reduced period of the perturbations are evident on nearly all time series in the dataset; four such time series are featured in Figure 3b-e.

We estimate wave propagation velocities using the slope of observed TECu amassed from all available satellites and 818 receivers on a distance-time plot (Figure 4). A faint disturbance arrives earliest propagating toward the volcano; we speculate that this was generated by Cyclone 04F near the Cook Islands and is irrelevant to this study. The supersonic acoustic TID, the first eruption-related perturbation, travels at 833 m/s between 1600 km and ~3000 km from Hunga. This velocity falls between those recently published (Matoza et al., 2022; Themens et al., 2022; Zhang et al., 2022), and one could argue for several different supersonic speeds depending on the specific location of the TID. Between ~3000-3500 km, this pulse decreases in velocity before returning to nearly 833 m/s, also observed by Themens et al. (2022) and Zhang et al. (2022). The Lamb wave TID then arrives at 310 m/s, followed minutes later by the initial tsunami TID at the same velocity, which is validated by DART arrivals. Beginning at ~08:00 UTC, enhanced tsunami-generated TIDs arrive at a velocity of 463 m/s.

In Figure 4b, we show the interpolated distance-time plot, which more clearly displays the distinct phase arrivals in the ionosphere. Interpolation was computed with a weighted average using two-dimensional Gaussian distance weighting with decay coefficients of 50 km and 30 s (e.g., Crowell et al., 2013). Within the interpolated data, an interesting TID emerges that is more challenging to locate within the raw data. Though the initial tsunami travels at 310 m/s, we see a TID moving at 463 m/s just behind the initial tsunami from ~2000-2800 km. By projecting the 463 m/s line to zero distance, there is a 1-hour difference between the initial volcanic eruption and the generation of the initial tsunami at ~2000 km. If the tsunami is generated at speeds coincident with the Lamb wave, the faster traveling tsunami emerges at ~1100 km from the volcano, which is around the distance of RAUL (i.e., Figure 2b). Indeed, for satellite G10 at RAUL, we do not see full separation of the higher frequency tsunami signal and the preceding Lamb wave, but there is a shift toward shorter periods from 05:30 to 06:00 (Figure 2e). While we do not have a definitive explanation for the generation of this faster traveling tsunami wave, we speculate that this could be generated by local bathymetry (or wave guiding along the Kermadec trench), a secondary source, or excitation from the supersonic acoustic wave. Furthermore, when the 310 and 463 m/s lines cross at ~2900 km, we see an additional amplification in the TEC signal potentially due to constructive interference. Moreover, the secondary crossing of these lines at 4500-5000 km leads to additional enhancement of the TEC signals.

By rotating the interpolated data in Figure 4b to explore TIDs relative to the arrival of tsunami-generated perturbations (Figure 5a), it is evident that TIDs before the initial tsunami have a longer period than those arriving after it. Slices taken at 2000 km, 2250 km, and 2500 km from

Hunga reinforce this observation (Figure 5b-d). Furthermore, looking at records from the DART buoys at these locations, we see much more high frequency signal after the tsunami's TID arrival than before, where the low frequency supersonic signal causes a low frequency response on the DART buoy. Following the tsunami's arrival, the speed of high frequency waves in the ionosphere appears to be roughly identical and certainly not slower than 463 m/s.

Given that Hunga's AG waves were powerful enough to generate a small tsunami in the Caribbean - an entirely different ocean basin with no direct path between them - it can be assumed that those same AG waves enhanced tsunami behavior in the Pacific. Generation of the initial tsunami wave can be tied in part to the propagation of the Lamb wave, which is only seen in extremely powerful eruptions and explosions such as Krakatoa's 1883 eruption (Harkrider & Press, 1967). Atmospheric influencing is demonstrated in our data as an abrupt change in frequency between Lamb- and tsunami-generated disturbances. This sudden compression of ionospheric perturbations likely appears due to coupling of AG waves with water gravity waves, during which ocean waves are excited by the large atmospheric pressure wave - even across continental land masses - and then build due to resonance from similar phase velocities of the lower atmosphere and ocean surface (Kubota et al., 2022; Press & Harkrider, 1966). Certainly, we see the effect of this process in our data via increased tsunami velocities and amplitudes as time progresses.

4. Conclusions

The Hunga event is highly unique and provides ample opportunity to explore many facets of submarine volcanism, as well as the mechanics of air-sea coupling and eruption- and tsunami-generated wave propagation into the ionosphere. Perhaps most importantly, it also provides a motivation to improve tsunami early warning systems. Due to the rapid velocity of tsunami waves, near-field warnings are often insufficient even without atmospheric enhancement of the waves. With atmospheric forcing, however, warnings were behind by hours in many areas; with a larger tsunami, this could lead to far greater loss of life in future events. By considering atmospheric influences from this event, we can better prepare for anomalous tsunami behavior in the future.

Acknowledgements

This work is funded through the NASA Disasters program, grant number 80NSSC19K1104 to BWC at University of Washington. Additionally, JNG is funded through the National Science Foundation Graduate Research Fellowship Program.

Data Availability Statement

All raw GNSS data is publicly available at GNS (https://data.geonet.org.nz/gnss/rinex/), UNAVCO (ftp://data-out.unavco.org/pub/rinex/obs/), CDDIS (https://cddis.nasa.gov/archive/gnss/data/daily), and Geoscience Australia (ftp://ftp.data.gnss.ga.gov.au/). The SNIVEL_ION code is freely available at https://github.com/crowellbw/SNIVEL_ION. DART data from New Zealand was accessed through the GEONET FDSN API (https://www.geonet.org.nz/data/tools/FDSN). NOAA DART data was obtained through their event response page (https://www.ngdc.noaa.gov/hazard/dart/2022tonga.html). All of the ionospheric waveforms used in this study are available on Zenodo (https://doi.org/10.5281/zenodo.6568025).

References

Astafyeva, E. (2019). Ionospheric detection of natural hazards. *Reviews of Geophysics*, 57, 1265-1288. https://doi.org/10.1029/2019RG000668

Astafyeva, E., Maletckii, B., Mikesell, T. D., Munaibari, E., Ravanelli, M., Coisson, P., Manta, F., et al. (2022). The 15 January 2022 Hunga Tonga eruption history as inferred from ionospheric observations. *Geophysical Research Letters*. https://doi.org/10.1029/2022GL098827

Carvajal, M., Sepulveda, I., Gubler, A., & Garreaud, R. (2022). Worldwide signature of the 2022 Tonga volcanic tsunami. *Geophysical Research Letters*, 49. https://doi.org/10.1029/2022GL098153

Coster, A., Herne, D., Erickson, P., & Oberoi, D. (2012). Using the Murchison Widefield Array to observe midlatitude space weather. *Radio Science*. 47. https://doi.org/10.1029/2012RS004993

Crowell, B. W., Bock, Y., Sandwell, D. T., & Fialko, Y. (2013). Geodetic investigation into the deformation of the Salton Trough. *Journal of Geophysical Research: Solid Earth*, 118(9), 5030-5039. https://doi.org/10.1002/jgrb.50347

Crowell, B. W. (2021). Near-field ground motions from GPS-derived velocities for 2020 Intermountain Western United States earthquakes. *Seismological Research Letters*, 92(2A), 840-848. https://doi.org/10.1785/0220200325

Dautermann, T., Callais, E., & Mattioli, G. (2009). Global positioning system detection and energy estimation of the ionospheric wave caused by the 13 July 2003 explosion of the Soufriere Hills volcano, Monserrat. *Journal of Geophysical Research*, 114(2), 1-15. https://doi.org/10.1029/2008JB005722

Ghent, J. N., & Crowell, B. W. (2022). Spectral characteristics of ionospheric disturbances over the Southwestern Pacific from the January 15, 2022 Tonga eruption and tsunami [Data set]. Zenodo. https://doi.org/10.5281/zenodo.6568025

Gusman, A. R., & Roger, J. (2022). Hunga Tonga - Hunga Ha'apai volcano-induced , sea level oscillations and tsunami simulations. GNS Science webpage, Accessed at https://doi.org/10.21420/DYKJ-RK41 on April 14, 2022.

Harkrider, D., & Press, F. (1967). The Krakatoa air-sea waves: An example of pulse propagation in coupled systems. *Geophysical Journal of the Royal Astronomical Society*, 13, 149-159. https://doi.org/10.1111/j.1365-246X.1967.tb02150.x

Hines, C. O. (1972). Gravity waves in the atmosphere. *Nature*, 239, 73-78. https://doi.org/10.1038/239073a0

Huang, C. Y., Helmboldt, J. F., Park, J., Pederson, T. R., & Willemann, R. (2019). Ionospheric detection of explosive events. *Reviews of Geophysics*, 57, 78-105. https://doi.org/10.1029/2017RG000594

Klobuchar, J. (1987). Ionospheric Time-Delay Algorithms for Single-Frequency GPS Users. *IEEE Transactions on Aerospace and Electronic Systems*, 3, 325-331. https://doi.org/10.1109/TAES.1987.310829

Kubota, T., Saito, T., & Nishida, K. (2022). Global fast-traveling tsunamis driven by atmospheric Lamb waves on the 2022 Tonga eruption. *Science*, 1-8. https://doi.org/10.1126/science.abo4364

Lamb, H. (1911). On atmospheric oscillations. *Proceedings of the Royal Society of London Series A*, 84, 551-572. https://doi.org/10.1098/rspa.1911.0008

Manta, F., Occhipinti, G., Hill, E., Perttu, A., Assink, J., & Taisne, B. (2021). Correlation between GNSS-TEC and eruption magnitude supports the use of ionospheric sensing to complement volcanic hazard assessment. *Journal of Geophysical Research: Solid Earth*, 126(2), 1-17. https://doi. org/10.1029/2020JB020726

Matoza, R. S., Fee, D., Assink, J. D., Iezzi, A. M., Green, D. N., Kim K., et al. (2022). Atmospheric waves and global seismoacoustic observations of the January 2022 Hunga eruption. Tonga. *Science*, 1-11. https://doi.org/10.1126/science.abo7063

Press, F., & Harkrider, D. (1966). Air-sea waves from the explosion of Krakatoa. *Science*, 154, 1325-1327. https://doi.org/10.1126/science.154.3754.1325

Savastano, G., Komjathy, A., Verkhoglyadova, O., Mazzoni, A., Crespi, M., Wei, Y., & Manucci, A. J. (2017). Real-time detection of tsunami ionospheric disturbances with a stand-alone GNSS receiver: A preliminary feasibility demonstration. *Scientific Reports*, Mar(7), 1-10. https://doi.org/10.1038/srep46607

Themens, D. R., Watson, C., Zagar, N., Vasylkevych, S., Elvidge, S., McCaffrey, A., et al. (2022). Global propagation of ionospheric disturbances associated with the 2022 Tonga volcanic eruption. *Geophysical Research Letters*, 49, e2022GL098158. https://doi.org/10.1029/2022GL098158

Zhang, S., Vierinen, J., Aa, E., Goncharenko, L. P., Erickson, P., Rideout, W., et al. (2022). 2022 Tonga volcanic eruption induced global propagation of ionospheric disturbances via Lamb waves. *Frontiers in Astronomy and Space Sciences*, Mar(9), 1-10. https://doi.org/10.3389/fspas.2022.871275

Figures

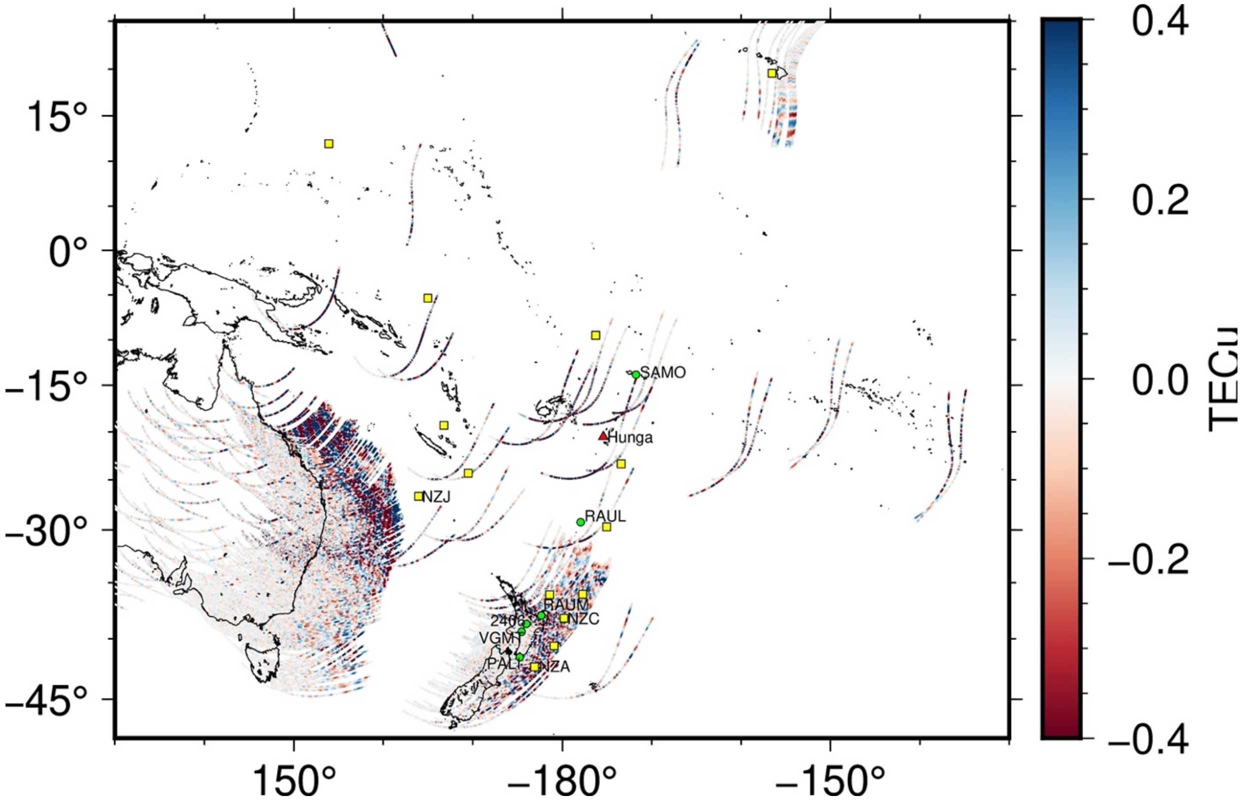

Figure 1. Mapview of ionospheric disturbance arrivals over southwestern Pacific for satellites G10 and G23. The general direction of satellite motion is from southwest to northeast between the time of eruption, 04:14 UTC, and 12:00 UTC on January 15, 2022. Yellow boxes represent the positions of DART buoys for which a first peak arrival is available. The red triangle denotes the location of Hunga. Green circles indicate the locations of GNSS stations that are discussed herein. TECu is saturated beyond +/- 0.4 to emphasize the locations of the strongest signals.

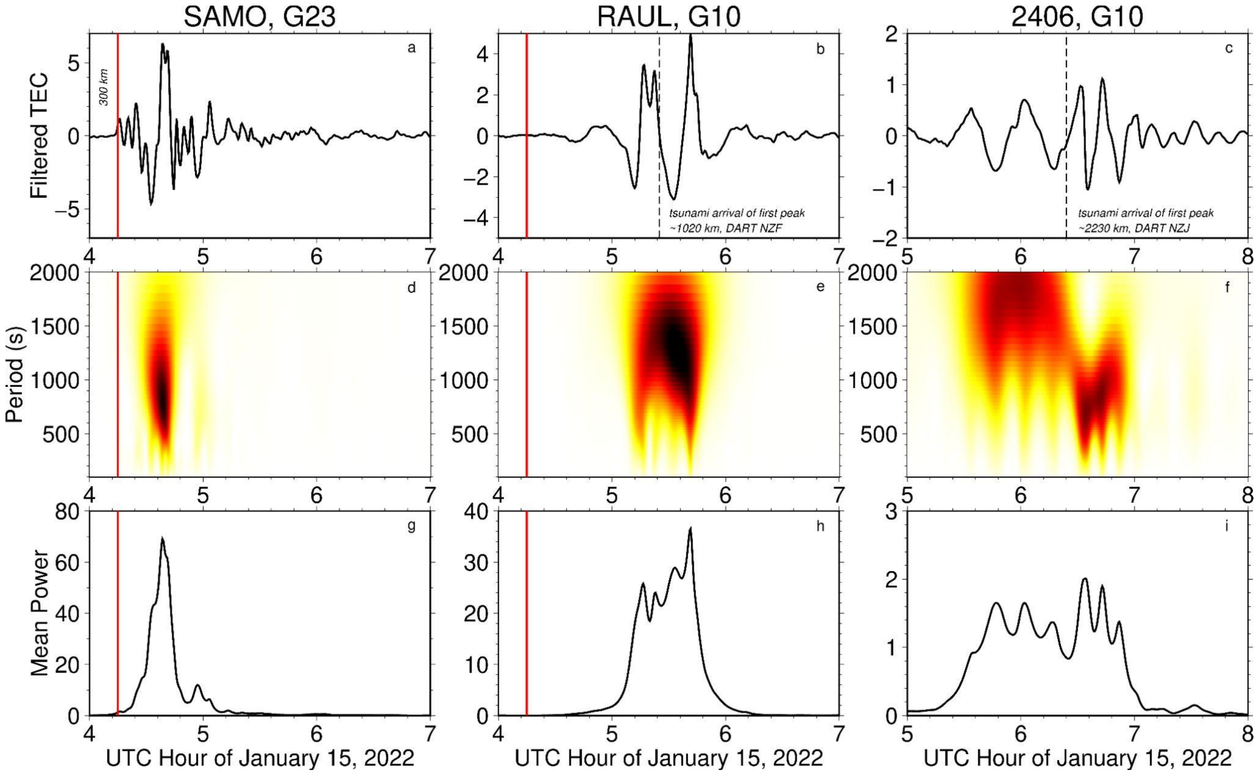

Figure 2. Comparison of ionospheric disturbances observed from the G23 satellite and SAMO receiver (a, d, g), the G10 satellite and RAUL receiver (b, e, h) and the G10 satellite and 2406 receiver (c, f, i) following the climactic January 15 eruption (red vertical line). Vertical black dashed lines represent the arrival of the tsunami's first peak as recorded by Gusman & Roger (2022). Mean power in (g-i) is the average power over all periods from the wavelet transform at a given time.

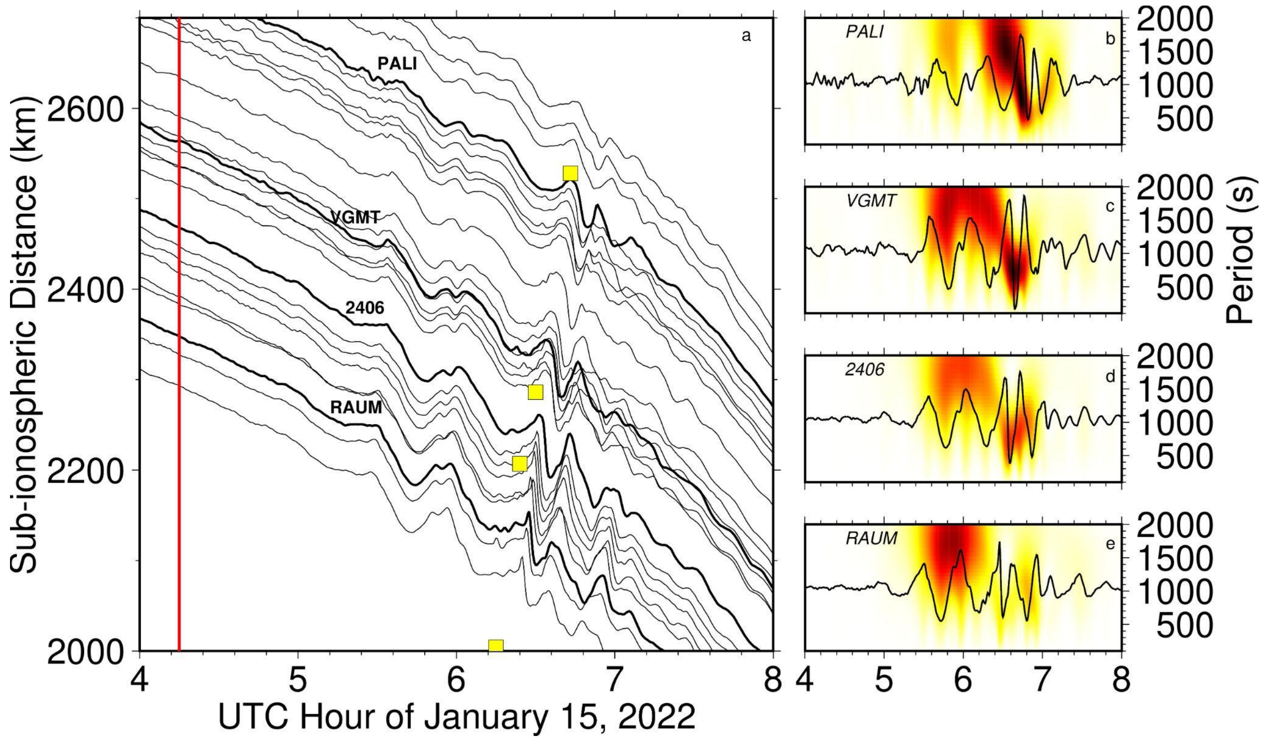

Figure 3. (a) Distance-time moveout of ionospheric disturbances following the eruption. Each moveout line represents a disturbance time series as recorded by a single receiver and satellite, plotted along the sub-ionospheric distance. Red vertical line is the eruption time, 04:14 UTC. All moveout lines here are observed by satellite G10. Bolded moveout lines correspond to the four time series/period plots (b-e), which emphasize the change in period as the AG wave is compressed. Yellow boxes represent the positions of DART buoys and timing of first tsunami peaks from Gusman & Roger (2022).

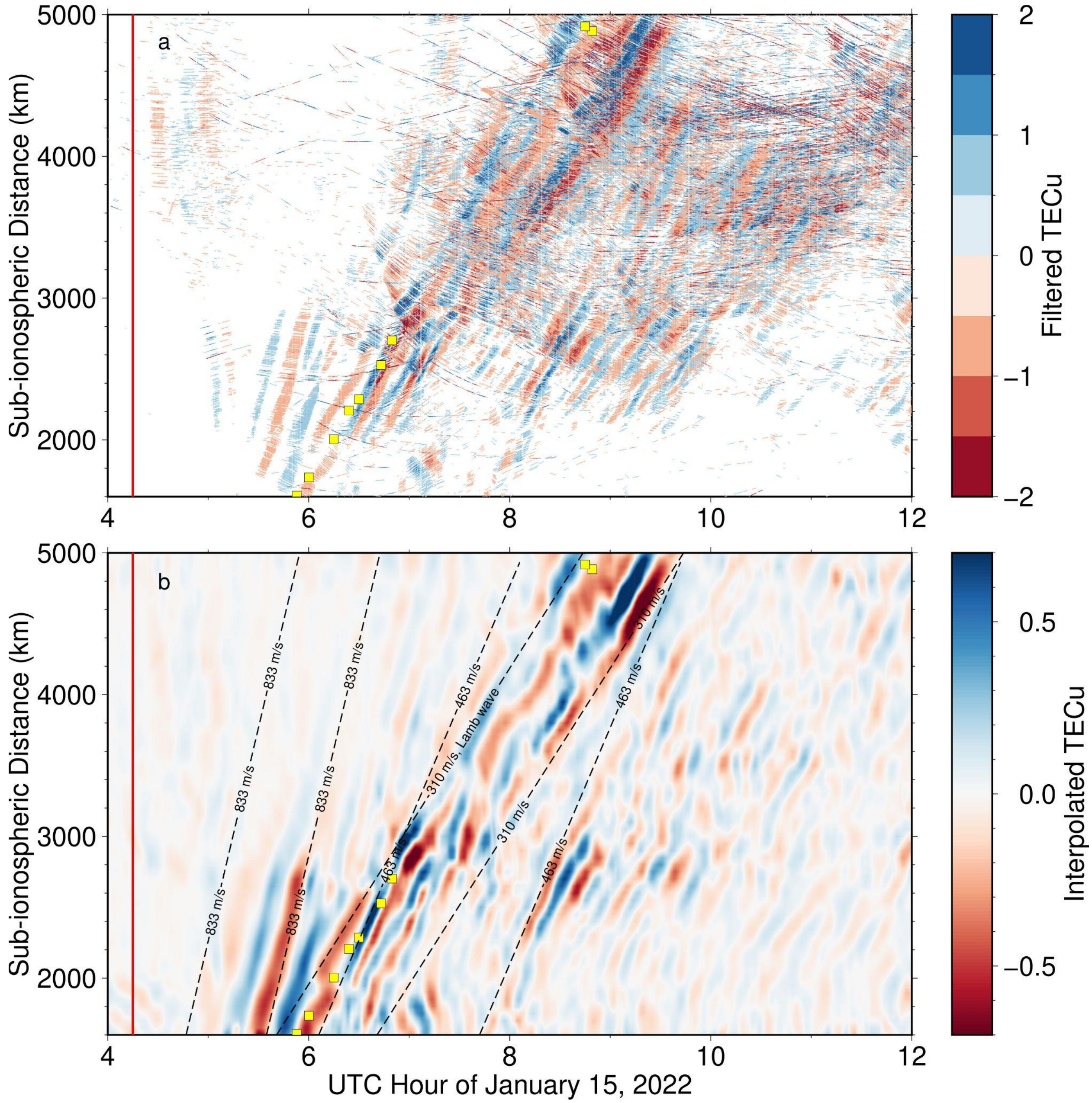

Figure 4. (a) Distance-time plot of total electron content from raw GNSS data. TECu is saturated beyond +/- 2 to emphasize locations of the strongest signals. Between +/- 0.5 TECu is excluded for clarity. For both panels, yellow boxes represent DART arrivals of the first peak in the initial tsunami wave from Gusman & Roger (2022). (b) Distance-time plots of total electron content from interpolated GNSS data. TECu is saturated beyond +/- 0.7 to emphasize locations of the strongest signals. Black dashed lines represent propagation velocities of TIDs. All data is included. An additional velocity of 463 m/s is included as a baseline for Figure 4.

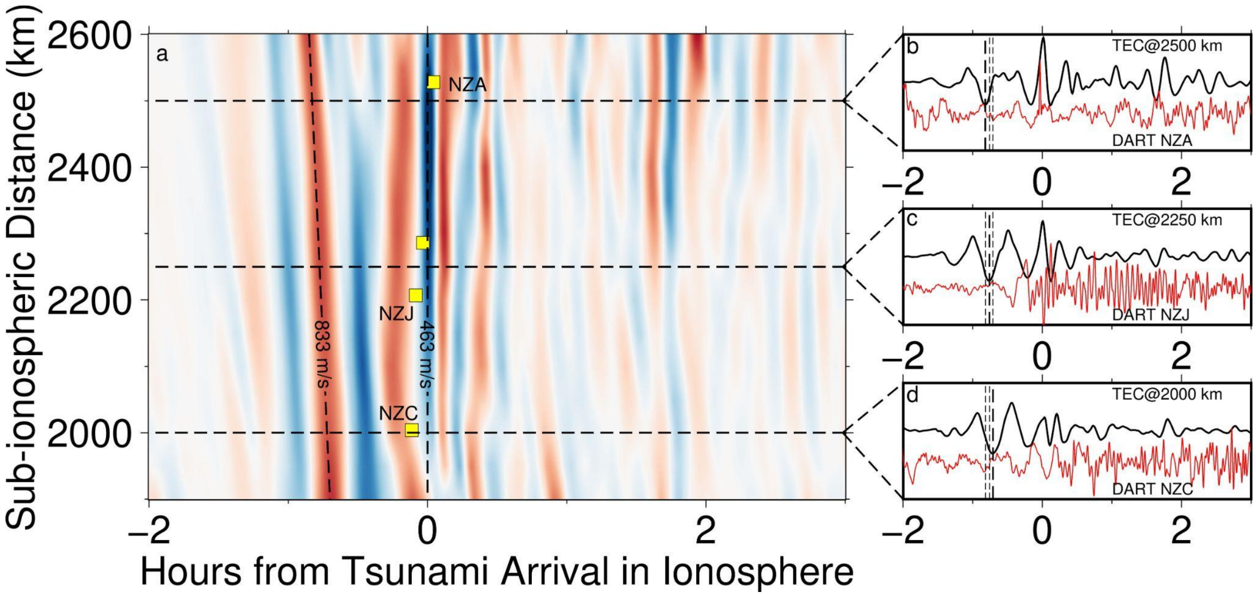

Figure 5. Rotated interpolated distance-time plot of total electron content to correspond with the first tsunami peak in the ionosphere (a), with slices at 2000 km, 2250 km, and 2500 km (b-d). Color scale of (a) is the same as Figure 4b. Arrival times of the first tsunami peak from Gusman & Roger (2022) are shown by the yellow squares. Vertical dashed lines in the sliced time series represent the minimum TECu that precedes initial tsunami arrival for all three slices, with bolded vertical dashed lines representing the minimum for a particular slice.